Journal of Applied Physics

Space charge in a vacuum diode: From macroscopic to microscopic gaps

Cite as: J. Appl. Phys. **130**, 024502 (2021); https://doi.org/10.1063/5.0053788
Submitted: 11 April 2021 . Accepted: 18 June 2021 . Published Online: 08 July 2021

Mohab O. Hassan, Kenichi Takahata, and Alireza Nojeh

Journal of Applied Physics ARTICLE scitation.org/journal/jap

Space charge in a vacuum diode: From macroscopic to microscopic gaps

Cite as: J. Appl. Phys. **130**, 024502 (2021); doi: 10.1063/5.0053788
Submitted: 11 April 2021 · Accepted: 18 June 2021 ·
Published Online: 8 July 2021

Mohab O. Hassan,[1,2] Kenichi Takahata,[1,a)] and Alireza Nojeh[1,2,a)]

AFFILIATIONS

[1]Department of Electrical and Computer Engineering, University of British Columbia, Vancouver, British Columbia V6T 1Z4, Canada
[2]Quantum Matter Institute, University of British Columbia, Vancouver, British Columbia V6T 1Z4, Canada

[a)]**Authors to whom correspondence should be addressed:** takahata@ece.ubc.ca and alireza.nojeh@ubc.ca

ABSTRACT

The space charge effect is important in free-electron devices and sometimes plays a key role. A vacuum-compatible micromanipulation platform was devised to study this effect in a diode structure while changing the width of the gap between the emitter and the collector *in situ* in the range of hundreds of micrometers to tens of micrometers. The current–voltage characteristics were found to upshift with a decrease in the interelectrode distance; the space charge-limited current increased by approximately two orders of magnitude when the interelectrode distance decreased from 550 to 50 μm. The simplicity of the parallel-plate structure enabled analysis based on one-dimensional emission and transport with the measurement results showing a good fit to the model by Longo combined with the Child–Langmuir theory.

I. INTRODUCTION

As it has been known for over a century now, in a charged-particle device, the space charge cloud can suppress further emission and transport, limiting the current density.[1,2] Space charge-limited (SCL) flow is important in cold and thermal electron emitters, various vacuum electronic devices, and plasma physics.[3,4] The space charge effect becomes particularly crucial and often detrimental when the charged particles move under a low or retarding external electric field, such as in thermionic energy conversion (TEC) devices.[5,6]

In its simplest form, one-dimensional SCL flow has been described by the classic Child–Langmuir (CL) law, which gives the maximum current density for steady state laminar flow between two wide, parallel electrodes—the emitter (also known as cathode in the case of electrons) and the collector (also known as anode in the case of electrons)—at a given distance from one another in vacuum and under a potential difference.[1–5,7,8] According to the original CL formula, the current density scales as the three-halves power of the potential difference and the inverse squared of the width of the inter-electrode gap. There have been various efforts to improve on the classic CL law, such as the study of the transition from emission mechanism-limited to SCL flow and extension to higher dimensions and the quantum regime.[3,4,9–13] Studies have dealt with space charge in both field-emitters (originally described by Fowler–Nordheim tunneling)[14–17] and thermionic emitters (originally described by the Richardson–Laue–Dushman law).[5–7,18–24]

Space charge mitigation has received particular attention in TEC devices in recent times since TEC conversion efficiency suffers directly from the space charge effect. The simplest proposed approach to space charge mitigation, which does not require the introduction of positive ions or gate electrodes, is directly inspired by the CL law; with a microscale or smaller interelectrode gap, the current predicted by the CL formula increases to the point that it practically no longer poses a limit.[25–28] For example, there have been experimental efforts to create thermally insulating spacers in order to enable microscale interelectrode gaps in thermionic devices.[22,29] Nanofabrication techniques have also made it possible to achieve interelectrode distances in the range of a few micrometers in SiC-based devices.[21,30] These studies have compared the output currents at a few interelectrode distances, set *ex situ*, in order to mitigate space charge. However, experimental conditions and device parameters can be unintentionally altered from one experiment to the next; for example, the emitter surface properties are prone to change due to exposure to air. In a relatively recent

study, an interelectrode gap control system was implemented to mitigate space charge in a TEC device with a dispenser cathode composed of a tungsten matrix-impregnated barium compound and a back-gated graphene anode.[23] The goal was to increase TEC efficiency, and promising results were demonstrated by reducing the work function of the graphene anode through electrostatic gating. However, the experimental conditions of that work were not directly relevant to the CL law: the area of the collector was significantly smaller than that of the emitter, which precludes a one-dimensional description of electron flow, and the ongoing presence of Ba adds to the complexity of charge transport dynamics in the interelectrode space.

In summary, surprisingly, a systematic experimental investigation of the CL law has so far been lacking at sub-millimeter interelectrode distances, which are increasingly important in modern vacuum electronic devices. Here, we present such an investigation. We created a vacuum-compatible platform for controlled, *in situ* variation of the width of the interelectrode gap from hundreds of micrometers to tens of micrometers. An yttria-coated iridium disk was used as the thermionic emitter for the device. The experimental results showed that the output current of the device gradually increased by two orders of magnitude by decreasing the interelectrode distance from 550 to 50 μm. Additionally, it was observed that the one-dimensional CL formula augmented by Longo's model,[19,31] which can also describe the transition from the space charge to the accelerating region, provided a good fit to the measurement data. This work, presents a decisive demonstration of space charge reduction confirming the CL picture in its simplest form in this miniaturized gap range.

II. EXPERIMENTAL METHODOLOGY

A. Emitter and collector

The emitter is an yttria-coated iridium disk (ES-529, Kimball Physics Inc., NH, USA) with a diameter of 1.57 mm, connected to two thin iridium terminal legs and can operate at even up to moderate vacuum levels of 1×10^{-4} Torr. The yttria coating covers the top surface of the disk but not its edges, which makes edge emission negligible due to the much higher work function of iridium compared to yttria. It is reported by the manufacturer that yttria has a Richardson constant of 5×10^{4} Am^{-2} K^{-2} and a work function of 2.6 eV at an operating temperature of 1800 K. The collector is made of a tungsten sheet with a thickness of 200 μm and lateral dimensions of 10×10 mm^2.

B. Variable interelectrode distance platform

The variable interelectrode distance platform consists of four main components: the linear actuator, the emitter holder, the collector holder, and the spring-loaded rods (Fig. 1). The vacuum-compatible motorized DC servo linear actuator (Z812V, Thorlabs Inc., NJ, USA) is modified to fit into the platform. The emitter holder is a standalone modular piece fixed to the platform body; it can be interchanged to fit different emitter types and sizes. The spring-loaded rods are actuated by the linear actuator and allow for bidirectional variation of the interelectrode distance. The collector holder is attached to the spring-loaded rods, which move the collector away from or toward the emitter while the emitter holder remains stationary, thus increasing or decreasing the interelectrode distance, respectively.

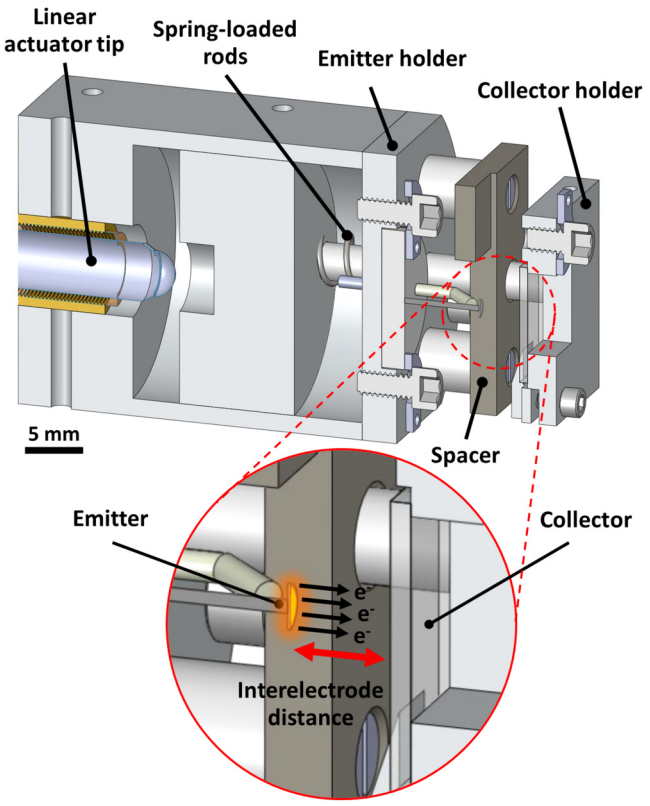

FIG. 1. A cross-sectional view of the variable interelectrode distance platform. The close-up inset shows the region between the surfaces of the emitter and the collector.

The actuator is rated at vacuum levels down to 1×10^{-6} Torr and has an inherent step size of 29 nm. The overall platform is tested in varying the interelectrode distance with a minimum step size of 1 μm. The smallest achievable interelectrode distance depends on the surface roughness of the emitter itself, while the largest achievable distance is 3 mm.

C. Electron emission and transport characterization apparatus

The apparatus used for the thermionic emission experiments is schematically shown in Fig. 2. The yttria-coated cathode is first attached to the emitter holder and aligned such that the top surface of the yttria coating is level with the surface of the spacer upon which two sides of the collector rest in the minimum interelectrode distance position but without electrical contact between the two electrodes (Fig. 1). The emitter holder is then fixed onto the platform, which is inserted into a vacuum chamber equipped with a turbomolecular pump (Turbo-V 81-M, Agilent, CA, USA).

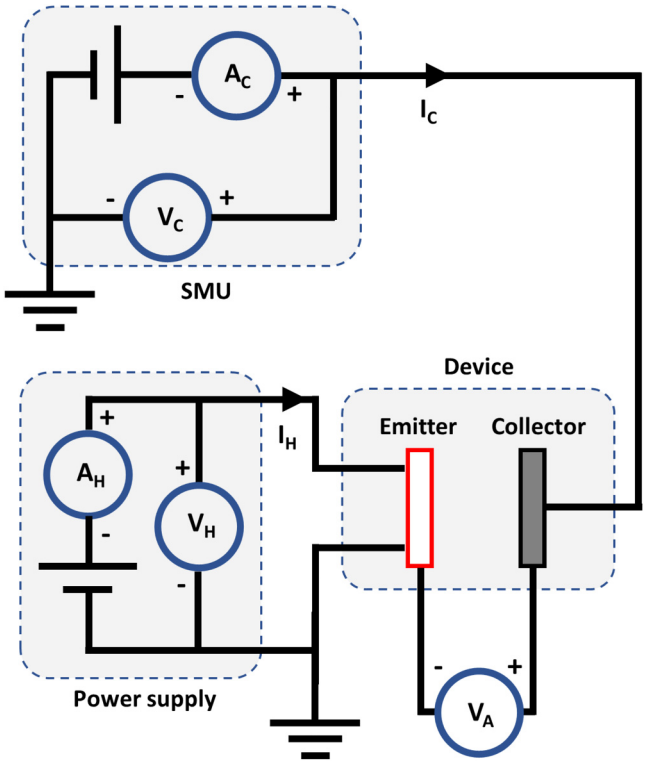

FIG. 2. A schematic of the thermionic emission and transport characterization apparatus. V_C and I_C stand for collector voltage and current, respectively, and V_H and I_H stand for emitter heating voltage and current, respectively. Assuming an equal voltage drop on both iridium disk heater legs, the applied voltage across the device (V_A) is equal to V_C–V_H/2.

The vacuum level measured by the gauge placed in the chamber is 1×10^{-7} Torr, although the pressure near the platform and the diode structure could be somewhat higher and likely closer to 1×10^{-6} Torr (as expected based on the rating of the actuator). A source-measure unit (SMU) (B2902A, Keysight Technologies, CA, USA) is used to apply a voltage in the range of −5 to +200 V to the collector while keeping one terminal of the emitter grounded. A DC voltage source (XFR 40-30, Xantrex, BC, Canada) is used to supply a power of up to 8.5 W to heat the iridium disk. A thermographic camera (VarioCAM, Jenoptik, Germany) is used to monitor the temperature of the side of the yttria-coated iridium disk while the interelectrode distance is being varied, as the top surface is not accessible due to its close proximity to the opaque collector (tungsten sheet) surface. As an example, an emitter temperature of 1700 K is measured with the iridium disk heater drawing 5.0 A of current at an applied heating voltage of 1.7 V, while the emitter and collector are at a distance of 50 μm from each other. In separate experiments meant to verify the emitter properties, a disappearing-filament pyrometer (Mikro Type PV 11, Keller ITS, Germany) is used in a structure with a fixed interelectrode distance of 2.3 mm with the same yttria-coated iridium disk as the emitter but a transparent collector (indium-tin-oxide coated glass).

A Matlab script is used to communicate with the actuator controller and SMU simultaneously in order to vary the interelectrode distance and record the collector current. The data are obtained by performing a collector voltage sweep typically from −5 to +100 V and measuring the collector current at each interelectrode distance, while stepping the actuator with a step size of 20 μm. Another Matlab script is used to implement a proportional-integral-differential (PID) controller for the heating power delivered to the iridium disk.

III. RESULTS AND DISCUSSION

A. Emitter characterization

The emitter's properties were verified by varying its temperature using the heating power supply and obtaining the corresponding zero-field collector current. The heating power was varied from 6.4 to 8.5 W, and the applied voltage was swept from −5 to +200 V with a step size of 1 V. The pyrometer was used to measure the emitter surface temperature as shown in Fig. 3(a). The measured current–voltage characteristics corresponding to each temperature are plotted in Fig. 3(b). As seen on the figure, the accelerating region did not exhibit a horizontal plateau; it was enhanced by the Schottky effect, that is, the lowering of the potential barrier at the emitter surface due to the applied field. This enhanced current region was extrapolated to obtain the zero-field current as shown in Fig. 3(b). The Richardson constant (5×10^4 Am^{-2} K^{-2}) and work function (2.6 eV) values given by the manufacturer of the yttria cathode yielded a good fit to the experimental data as shown in the Richardson plot [inset of Fig. 3(b)] constructed from the zero-field current values. This serves as a confirmation of these values for the Richardson constant and work function, which will be important parameters in data fitting and analysis later.

B. Interelectrode distance variation

The platform was tested to confirm the step size, bidirectionality, and interelectrode alignment. Movement steps of 1, 5, 10, and 100 μm were tested, and an accuracy of ±1 μm in the desired actuated distance was obtained. The backlash of the linear actuator itself is listed in the manufacturer specifications as <8 μm. However, the spring-loaded mechanism in the platform reduced this backlash to a negligible level compared to the 20 μm step size later used in the thermionic experiments.

The interelectrode distance and the electrode temperatures were continuously monitored during the experiments using the thermographic camera looking at the device from the side. With the aid of an optical microscope, the two electrodes were verified to be aligned through visual inspection at the beginning and the end of the experiment (Fig. 4). At the beginning of an experiment, in order to calibrate the interelectrode distance, the collector was slowly moved toward the emitter until it barely touched the highest crests of the yttria coating as judged through the optical microscope but without electrical contact being made between the two electrodes. This defined the minimum interelectrode distance to be ~50 μm (as will also be substantiated by fitting to the model in Sec. III C).

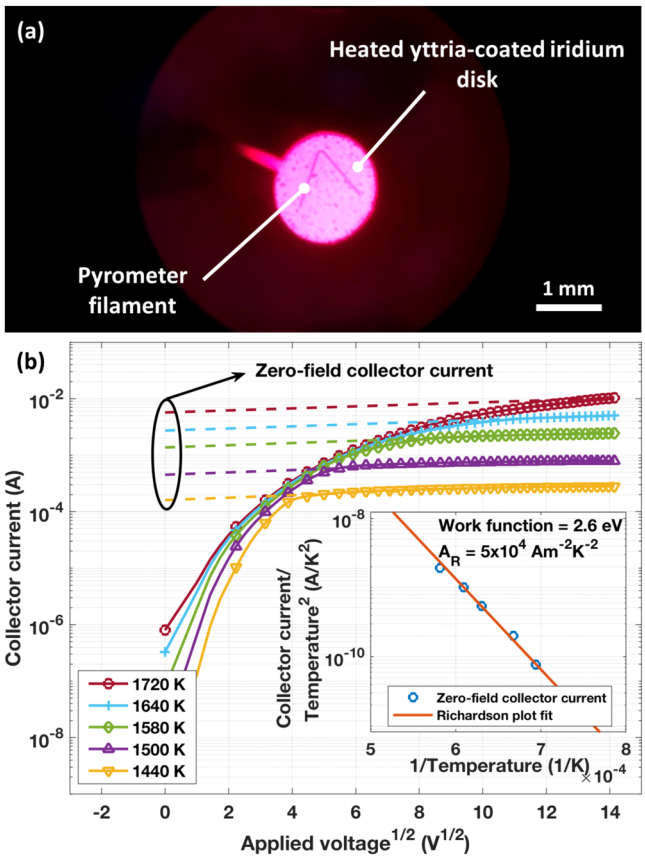

FIG. 3. Emitter surface characterization. (a) An image taken through the eyepiece of the pyrometer showing the pyrometer filament and the heated disk inside the vacuum chamber. The filament temperature was made to be slightly lower than the emitter so that it is visible on the image. (b) Current–voltage characteristics taken at different temperatures were used to construct the Richardson plot (inset). A Richardson constant of 5×10^4 Am^{-2} K^{-2} and a work function of 2.6 eV were confirmed by this plot.

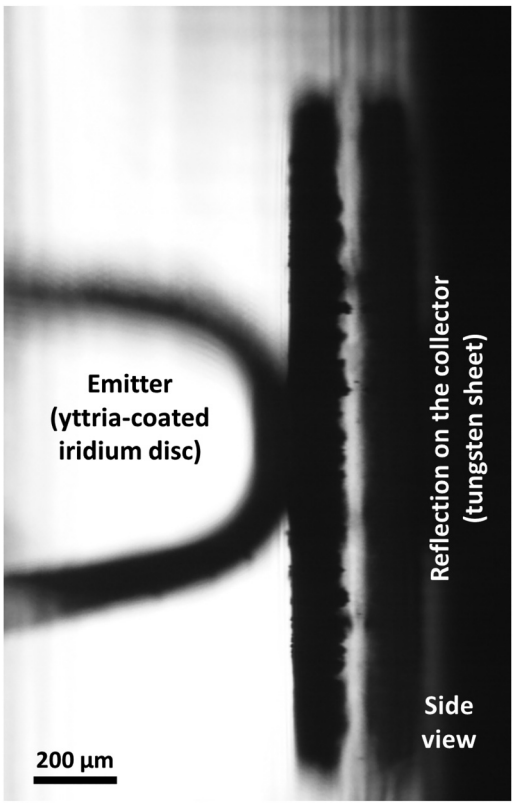

FIG. 4. An optical microscope image showing the alignment of the emitter (yttria-coated iridium disk) surface with the collector (tungsten sheet) surface. The roughness of the yttria coating is ~50 μm.

C. Thermionic emission and transport measurements and modeling

The collector current was measured as a function of the differential voltage applied between the collector and the emitter at different interelectrode distances, starting at 550 μm and decreasing to 50 μm with a step size of 20 μm. The current–voltage characteristics (Fig. 5) exhibited the three regions of operation of a typical thermionic device, i.e., retarding, space charge, and accelerating regions. The retarding and space charge regions are separated by the critical voltage, whereas the space charge and accelerating regions are separated by the saturation voltage. These specific voltage values will be highlighted later in the theoretical model.

In the accelerating region, the collector current did not exhibit a horizontal plateau, which was again a manifestation of the Schottky effect. The yttria coating crests may have exacerbated this effect by providing electric field enhancement near the emitter surface. Interestingly, the saturation current increased with decreasing the interelectrode distance. This can be explained by the fact that the emitter temperature was found to increase by approximately 250 K as the collector moved to vary the interelectrode distance from 550 to 50 μm. This effect was found to be repeatable and reversible. It is conceivable that, at smaller interelectrode distances, the collector surface was reflecting more thermal energy to the emitter. (It is worth recalling that the electric power delivered to the emitter was controlled to be essentially constant, fluctuating by less than 0.5%, throughout the experiment.) Regardless of the cause, this change in the emitter temperature was taken into account in the model presented later. Moreover, as shown in Fig. 5, the saturation voltage, which defines the beginning of the accelerating region, was found to increase as the interelectrode distance was increasing, as expected. However, this increase is relatively small because the emitter temperature decreased as the interelectrode distance increased.

In the retarding region, the collector current was found to exhibit a straight line on the logarithmic scale (Fig. 5). It may be counter intuitive that the retarding region extended into positive applied voltages. However, this is due to the potential barrier in the interelectrode space caused by the space charge effect in the first

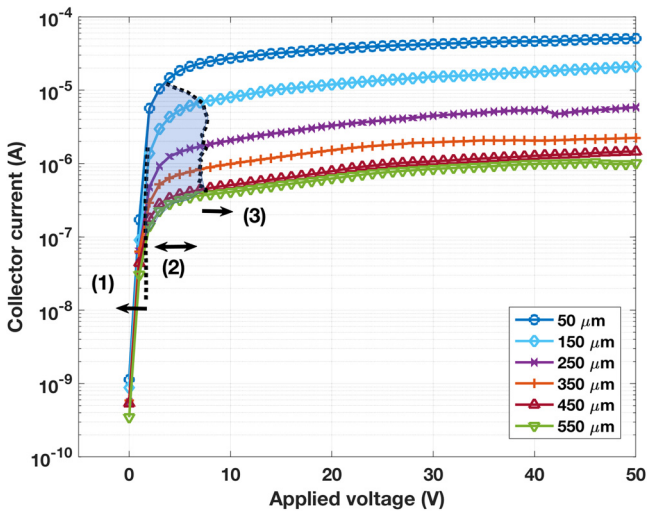

FIG. 5. Current–voltage characteristics of the device at select interelectrode distances. The three regions (1, 2, and 3) in the figure correspond to the retarding, space charge, and accelerating (with the Schottky effect) regions, respectively. The space charge region (2) is shaded to visually distinguish it from the other regions.

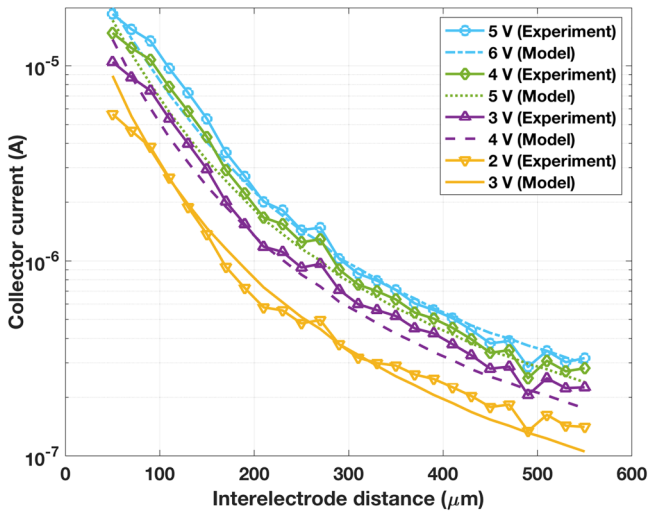

FIG. 6. The measured (lines with markers) device current vs the interelectrode distance in the space charge region (applied voltage = 2, 3, 4, and 5 V). The model results (lines without markers) are also plotted (applied voltage = 3, 4, 5, and 6 V), exhibiting good agreement with the measured values. There is a 1 V difference between the experimental applied voltage and the model applied voltage.

place, which repels the emitted electrons even when the collector is at a slightly positive voltage.

We now turn to the space charge region. In order to highlight the key result, Fig. 6 shows the measured current vs the interelectrode distance at applied voltages of 2, 3, 4, and 5 V, all of which fall within the space charge region. (The model fits on the figure will be discussed later.) The current increased nonlinearly by about two orders of magnitude as the interelectrode distance decreased to its minimum, which is qualitatively consistent with the CL theory of space charge. However, the CL picture implies an abrupt transition from the space charge to the accelerating region once the CL value of the current exceeds the Richardson–Laue–Dushman value. Instead, we observed a smooth transition in all curves (Fig. 5). This is in line with Longo's model,[19,31] which describes the intermediate region between space charge and accelerating, with those two regions forming limiting cases. This model has been used previously to fit experimental data[32,33] but without considering the effect of the interelectrode distance. In general, it is expected from a comprehensive electron emission and transport theory to predict a smooth transition between the two regions. More recent models have also been developed to describe the smooth transition between the space charge and accelerating regions.[7,34,35] However, we note that our experimental design was meant to probe the space charge effect in its most basic form, and the simple Longo model will be sufficient for our analysis as will be seen below.

The lateral dimensions of the emitter and collector (1.57 mm in diameter and $10 \times 10\ \text{mm}^2$ in side length, respectively) had been chosen to be significantly larger than the widest interelectrode distances to be studied in this work ($550\,\mu$m). This choice was intended to enable analysis based on one-dimensional (1D) emission and transport, in order to provide access to the core behavior of the space charge effect, free of complications arising when emission and transport involve a significant 2D or 3D nature. The Richardson–Laue–Dushman current density can, therefore, be used and is expressed as

$$J_S = A_R T_E^2 \exp\left(\frac{-(\phi_E - \Delta\phi)}{k_B T_E}\right), \quad \left(\Delta\phi = \sqrt{\frac{e^3\beta(V - V_{Sat})}{4\pi\epsilon_o d}}\right), \tag{1}$$

where A_R is the Richardson constant, T_E is the emitter temperature, ϕ_E is the emitter work function, k_B is the Boltzmann constant, $\Delta\phi$ is the reduction in the emitter work function because of the Schottky effect, e is the electron charge, β is a geometric enhancement factor due to the surface roughness of the electrodes, V_{Sat} is the saturation voltage, ϵ_o is the permittivity of free space, and d is the interelectrode distance. This current density defines the accelerating region. In the space charge region, the CL current density is expressed as

$$J_{SC} = \frac{4\sqrt{2}}{9}\epsilon_o\left(\frac{e}{m_e}\right)^{1/2}\frac{|V - V_{Crt}|^{3/2}}{d^2}, \tag{2}$$

where m_e is the electron mass and V_{Crt} is the critical voltage. The critical voltage defines the onset of the space charge region and depends on the critical current density. According to Longo's

model,[19,31] the current density in the space charge and accelerating regions is given by the empirical asymptotic equation,

$$J_T = \frac{J_S J_{SC}}{J_S + J_{SC}}. \tag{3}$$

In the retarding region, the current density is given by the Boltzmann line equation,

$$J_R = A_R T_E^2 \exp\left(\frac{-(\phi_C - eV)}{k_B T_E}\right), \tag{4}$$

where ϕ_C is the collector work function and V is the applied voltage. The current density in both the accelerating and retarding regions can be obtained by direct substitution in Eqs. (1) and (4), respectively. The calculation of the current density in the space charge region is accomplished using Eqs. (2) and (3) but this requires knowledge of the critical voltage as needed by Eq. (2). This voltage is obtained through the procedure explained in detail in Refs. 5 and 36.

The above equations were used to fit the experimental data of Figs. 5 and 6 with the following model parameters: $A_R = 5 \times 10^4\ \mathrm{Am^{-2}\,K^{-2}}$ and $\phi_E = 2.6$ eV (as given by the manufacturer and verified in Sec. III A), $\phi_C = 4.0$ eV, emission spot diameter = 0.12 mm, interelectrode distance from 550 to 50 μm, and an increasing T_E from 1470 to 1700 K over this distance range. These parameters produced the best fit with the experimental results. To generate the model fits to the device current vs the interelectrode distance curves in Fig. 6, the IV curves for all the interelectrode gap widths (from 550 to 50 μm with a step size of 20 μm) were first obtained in different operating regions using Eqs. (1)–(4) with the fitting parameters mentioned above. Then, several applied voltage values were chosen to plot the experimental data vs the model data in the space charge region. In order to highlight the smooth transition from space charge to accelerating and illustrate the effect of Longo's model, in Fig. 7, we show one of the measured curves of Fig. 5 with model fits both without and with Longo's equation.

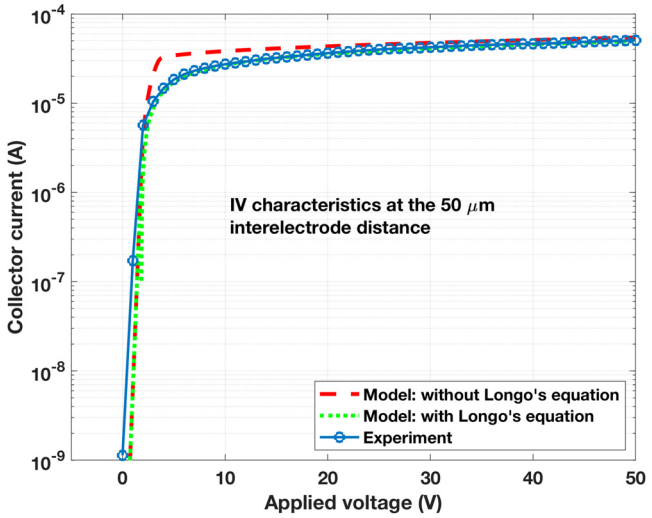

FIG. 7. A plot showing the difference between the smooth and sharp transitions predicted by the CL law with and without the inclusion of Longo's model, respectively, in comparison with the curve at 50 μm interelectrode distance obtained experimentally (reproduced from Fig. 5).

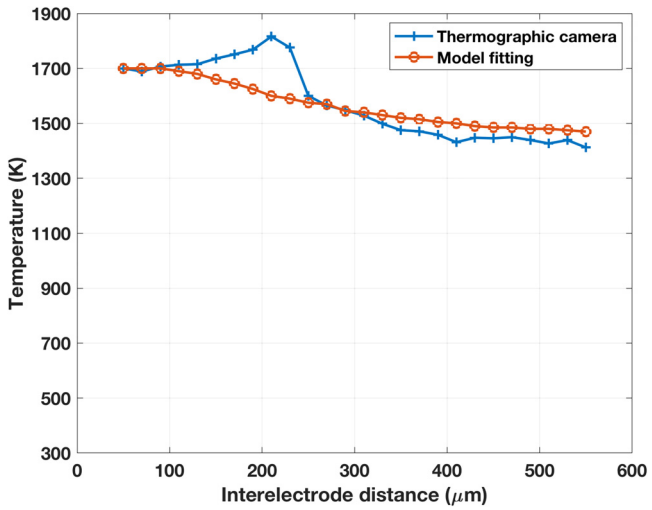

FIG. 8. The emitter temperature as a function of the interelectrode distance measured using the thermographic camera and extracted from the model.

The model parameters were, thus, in good agreement with the actual experimental parameters, except for the emission spot diameter of 0.12 mm in the model compared to the emitter disk size of 1.57 mm. This may be because the yttria coating did not cover the entire iridium disk uniformly. The smallest interelectrode gap width of 50 μm used in the model is consistent with the limitation imposed by the ~50 μm surface roughness of the emitter (Fig. 4). Similarly, the temperature increase over the entire gap range of 230 K needed by the model is in close agreement with the increase observed experimentally (250 K) using the thermographic camera (Fig. 8). The apparent peak in temperature observed experimentally around the 200 μm interelectrode distance might have been an artifact caused by optical reflection from the collector surface; it is to be noted that the saturation current increased monotonically as the interelectrode distance decreased (Fig. 5), which suggests a monotonic increase in temperature. Finally, Fig. 6 also shows the model fits to the measured currents as a function of interelectrode distance. (The 1 V difference between the experimental applied voltage and the model voltage may be attributable to an uneven distribution of the 1.7 V power supply voltage across the iridium disk heater.)

IV. SUMMARY AND CONCLUSIONS

The space charge effect has been studied by investigating the role of the interelectrode distance on the current in a vacuum diode using an yttria-coated iridium disk as the thermionic emitter and a tungsten sheet collector. A custom-made platform devised for *in situ* interelectrode distance variation was used for this purpose. The

measured device current in the space charge region increased by approximately two orders of magnitude as the width of the interelectrode gap decreased from 550 to 50 μm. A model by Longo based on the Child–Langmuir space charge theory provided a good fit to the experimental results. These results demonstrate that miniaturizing the interelectrode space is a very effective method to improve the output current and overcome the space charge effect. This is crucial in devices where the space charge effect is detrimental, such as thermionic energy converters, and increasingly important as vacuum electronic devices are pushed toward further miniaturization.

ACKNOWLEDGMENTS

We acknowledge financial support from the Natural Sciences and Engineering Research Council of Canada (Grant Nos. SPG-P 478867, RGPIN-2017-04608, and RGPIN- 2016-04252), the Canada Foundation for Innovation, and the British Columbia Knowledge Development Fund. This research was undertaken thanks in part to funding from the Canada First Research Excellence Fund, Quantum Materials and Future Technologies Program.

DATA AVAILABILITY

The data that support the findings of this study are available from the corresponding author upon reasonable request.

REFERENCES

[1]C. D. Child, Phys. Rev. **32**, 492 (1911).
[2]I. Langmuir, Phys. Rev. **2**, 450 (1913).
[3]P. Zhang, Á Valfells, L. K. Ang, J. W. Luginsland, and Y. Y. Lau, Appl. Phys. Rev. **4**, 011304 (2017).
[4]P. Zhang, Y. S. Ang, A. L. Garner, Á Valfells, J. W. Luginsland, and L. K. Ang, J. Appl. Phys. **129**, 100902 (2021).
[5]G. N. Hatsopoulos and E. P. Gyftopoulos, *Thermionic Energy Conversion* (MIT Press, Cambridge, MA, 1973).
[6]S. Meir, C. Stephanos, T. H. Geballe, and J. Mannhart, J. Renew. Sust. Energy **5**, 043127 (2013).
[7]D. Chernin, Y. Y. Lau, J. J. Petillo, S. Ovtchinnikov, D. Chen, A. Jassem, R. Jacobs, D. Morgan, and J. H. Booske, IEEE Trans. Plasma Sci. **48**, 146 (2020).
[8]I. Langmuir, Phys. Rev. **21**, 419 (1923).
[9]Y. Y. Lau, Phys. Rev. Lett. **87**, 278301 (2001).
[10]J. W. Luginsland, Y. Y. Lau, R. J. Umstattd, and J. J. Watrous, Phys. Plasmas **9**, 2371 (2002).
[11]W. S. Koh, L. K. Ang, and T. J. T. Kwan, Phys. Plasmas **12**, 053107 (2005).
[12]T. Lafleur, Plasma Sources Sci. Technol. **29**, 065002 (2020).
[13]L. K. Ang, W. S. Koh, Y. Y. Lau, and T. J. T. Kwan, Phys. Plasmas **13**, 056701 (2006).
[14]J. P. Barbour, W. W. Dolan, J. K. Trolan, E. E. Martin, and W. P. Dyke, Phys. Rev. **92**, 45 (1953).
[15]Y. Y. Lau, Y. Liu, and R. K. Parker, Phys. Plasmas **1**, 2082 (1994).
[16]R. G. Forbes, J. Appl. Phys. **104**, 084303 (2008).
[17]A. Rokhlenko, K. L. Jensen, and J. L. Lebowitz, J. Appl. Phys. **107**, 014904 (2010).
[18]C. K. Birdsall and W. B. Bridges, J. Appl. Phys. **32**, 2611 (1961).
[19]R. T. Longo, in *International Electron Devices Meeting* (IEEE, 1980), pp. 467–470.
[20]T. P. Lin and G. Eng, J. Appl. Phys. **65**, 3205 (1989).
[21]J. H. Lee, I. Bargatin, T. O. Gwinn, M. Vincent, K. A. Littau, R. Maboudian, Z.-X. Shen, N. A. Melosh, and R. T. Howe, in *25th International Conference on Micro Electro Mechanical Systems (MEMS)* (IEEE, 2012), pp. 1261–1264.
[22]K. A. Littau, K. Sahasrabuddhe, D. Barfield, H. Yuan, Z.-X. Shen, R. T. Howe, and N. A. Melosh, Phys. Chem. Chem. Phys. **15**, 14442 (2013).
[23]H. Yuan, D. C. Riley, Z.-X. Shen, P. A. Pianetta, N. A. Melosh, and R. T. Howe, Nano Energy **32**, 67 (2017).
[24]R. Wanke, W. Voesch, I. Rastegar, A. Kyriazis, W. Braun, and J. Mannhart, MRS Bull. **42**, 518 (2017).
[25]J. I. Lee, Y. H. Jeong, H.-C. No, R. Hannebauer, and S.-K. Yoo, Appl. Phys. Lett. **95**, 223107 (2009).
[26]J.-H. Lee, I. Bargatin, N. A. Melosh, and R. T. Howe, Appl. Phys. Lett. **100**, 173904 (2012).
[27]E. Rahman and A. Nojeh, Phys. Rev. Appl. **14**, 024082 (2020).
[28]E. Rahman and A. Nojeh, Energy **204**, 117947 (2020).
[29]S. M. Nicaise, C. Lin, M. Azadi, T. Bozorg-Grayeli, P. Adebayo-Ige, D. E. Lilley, Y. Pfitzer, W. Cha, K. Van Houten, N. A. Melosh, R. T. Howe, J. W. Schwede, and I. Bargatin, Microsyst. Nanoeng. **5**, 31 (2019).
[30]J.-H. Lee, I. Bargatin, B. K. Vancil, T. O. Gwinn, R. Maboudian, N. A. Melosh, and R. T. Howe, J. Microelectromech. Syst. **23**, 1182 (2014).
[31]R. T. Longo, AIP Adv. **9**, 085227 (2019).
[32]X. Yang, P. Wang, Z. Wang, K. Hu, H. Cheng, Z. Li, and J. Zhang, Mater. Des. **133**, 299 (2017).
[33]H. Wang, M. Li, and X. Liu, in *17th International Conference on High Power Particle Beams (BEAMS)* (IEEE, 2012), pp. 1–4.
[34]A. Jassem, D. Chernin, J. J. Petillo, Y. Y. Lau, A. Jensen, and S. Ovtchinnikov, IEEE Trans. Plasma Sci. **49**, 749 (2021).
[35]A. Sitek, K. Torfason, A. Manolescu, and Á Valfells, Phys. Rev. Appl. **15**, 014040 (2021).
[36]A. H. Khoshaman, A. T. Koch, M. Chang, H. D. E. Fan, M. V. Moghaddam, and A. Nojeh, IEEE Trans. Nanotechnol. **14**, 624 (2015).